Electronic Supporting Information (ESI) for

Surface phonons of lithium ion battery active materials

Peter Benedek[1], Nuri Yazdani[1], Hungru Chen[2], Nils Wenzler[1], Fanni Juranyi[3], Martin Månsson[4], M. Saiful Islam[2], Vanessa C. Wood[1].*

[1]Department of Information Technology and Electrical Engineering, ETH Zurich, CH-8092 Zurich, Switzerland

[2]Department of Chemistry, University of Bath, Bath BA2 7AY, United Kingdom

[3]Laboratory for Neutron Scattering and Imaging, Paul Scherrer Institute, CH-5232 Villigen PSI, Switzerland

[4]Department of Applied Physics, KTH Royal Institute of Technology, SE-164 40 Stockholm, Kista, Sweden

1. Detailed Experimental Methods

LFP Particle Synthesis

All $LiFePO_4$ samples were synthesized in a solvothermal reaction with ethylene glycol (EG, Acros) and distilled water as solvents. As a first step, enriched $^7Li_3PO_4$ (LPO) was synthesized. For this, aqueous solutions of $^7LiOH{\cdot}H_2O$ (>99.95% ^7Li, Nukem Chemicals) H_3PO_4 (Sigma) solution were prepared at concentrations of 3M for ^7LiOH or 1M for H_3PO_4, respectively. 400ml of both solutions were then mixed together and stirred for a few hours to equilibrate. LPO resulted as a white precipitate, which was filtered and washed with water. This LPO precursor powder was then used for all reactions.

The "Bulk" $LiFePO_4$ sample was made as described in an earlier publication.[1] For this, we dispersed the LPO powder in 40ml distilled water in a hydrothermal reactor of 50ml volume. We then added preground $FeSO_4{\cdot}7H_2O$ powder and EG to the solution to reach a precursor concentration of 0.8M and an EG concentration of 0.08M. The reactor was then closed, heated to 115°C with a heating mantle and kept at temperature for six hours while the mixture was

constantly stired. The resulting off-white powder was washed four times in water and once in ethanol.

Table S1 summarizes the reaction conditions for the “Meso”, “Medium”, “Nano” platelet particles which were prepared similarly to the “Bulk” particles, but with different temperatures and EG concentrations.

All the samples were coated with 3wt% Carbon. For this, we thoroughly ground D-Glucose (Sigma) with the LFP. After that, the mixture was pressed into pellets and annealed in Ar/2wt% H_2 at 600°C for 6h. The carbon coating was analyzed with a transmission electron microscope (FEI F30).

The preparation procedure of the delithiated LFP ($FePO_4$) particles is provided in the following section.

Table S1. Summary of the hydrothermal conditions.

Sample	**Nano**	**Medium**	**Meso**	**Bulk**
Reactor Temperature	180°C	180°C	180°C	115°C
Reaction Time	6h	6h	6h	6h
EG concentration	100v%	50v%	0.08mol/l	0.08mol/l
Precursor Concentration	0.5mol/l	0.8mol/l	0.8mol/l	0.8mol/l

Determination of Particle Dimensions

To determine the LFP particle dimensions, scanning electron microscopy (SEM) images in secondary electron mode were taken using a Hitachi SU-8200. The lengths and thicknesses of up to 500 particles were then measured using ImageJ. For the “Nano” sample, atomic force microscopy was performed with a Nanoscope Dimension 3100 AFM. As many of the nanoplatelets lie flat on the substrate, the z-deflection of the cantilever was used to determine the particle thickness.

Analysis of Structural Defects

FTIR spectra were obtained with a Bruker Vertex 70 in an attenuated total reflection setup with the LFP power placed on a Ge single crystal. The symmetric PO_4 stretching band was fit with a Gaussian function. X-ray powder diffraction spectra were measured in a 2ϑ range between 10° and 90° using a Rigaku Smart Lab diffractometer. Rietveld refinements were performed with Maud.[2]

Electrochemical Measurements

LFP electrodes were prepared by coating an N-methyl-2-pyrrolidone (NMP, Sigma) based slurry on an aluminum current collector. The slurry contained 70wt% active material, 20wt% carbon black (Timcal Super C65), and 10wt% polyvinylidene fluoride (Kynar HSV900). This lead to typical uncalendered dry active coating thicknesses of 40-60µm with variation due to the different tap densities of the samples and thus different viscosities in the slurries. A glass fiber separator, electrolyte consisting of 1M $LiPF_6$ in a 1:1 solution of ethylene carbonate and dimethyl carbonate (BASF), and a metallic lithium counter electrode completed the cell. Galvanostatic electrochemical analysis was performed on coin cells using the Astrol Bat-Flex potentiostat.

Inelastic Neutron Scattering (INS) Measurements and Analysis

INS measurements were performed at the FOCUS time-of-flight spectrometer at the neutron spallation source SINQ, Paul Scherrer Institute, Switzerland. For the measurement, 2-3g of sample material were added in a cylindrical Al holder made out of a thin layer of Aluminum foil. A neutron wavelength of 2.4Å (i.e., neutron energy of 14.2meV) was used. Data collection time was 8-10 hours per sample. The resulting data were reduced using the Dave software.[3] In the software, the background of the empty holder was subtracted and the detector efficiency was taken in account by normalisation to a vanadium standard having similar geometry as the samples. Finally, the phonon density of states was obtained using the MSlice environment in Dave, where the appropriate range of the scattering vectors Q was selected.

Simulations

$LiFePO_4$ phonon spectra were simulated based on the density functional perturbation theory[4] as implemented in VASP[5], in conjunction with the Phonopy code.[6] The electron exchange and correlation energy were described using the PBEsol functional.[7] Valence electrons were described using a plane wave basis set with a cutoff energy of 500eV. The interactions between valence and core electrons were treated using the projector augmented-wave (PAW) method.[8] The k-space was sampled with a k-point mesh with spacings smaller than 0.05 $Å^{-1}$.

Geometry calculations on LFP slabs (AIMD) were performed within the CP2K program suite utilizing the quickstep module.[9] Calculations were carried out using a dual basis of localized Gaussians and plane-waves[10] with a 300Ry plane-wave cutoff. Double-Zeta-Valence-Polarization (DZVP),[11] Goedecker–Teter–Hutter pseudopotentials[12] for core electrons, and the Perdew–Burke–Ernzerhof (PBE) exchange correlation functional were used. Convergence to 10^{-8} in Self-Consistent Field calculations was enforced. Electronic correlation within the *d* orbital of Fe was included through the $+U$ strategy with $U = 4.3$eV.[13,14]

Unit cell dimensions of [a, b, c] = [9.91, 6.095, 4.636]Å were determined through a cell optimization using a conjugate gradient optimization. LFP slabs are constructed with unit cell dimensions [100]x[010]x[001] = 1x3.5x2 in a simulation cell with dimensions [a, 35Å, 2c]. Periodic boundary conditions are used in all directions. All atoms in all systems are relaxed through geometry optimization, performed with the Quickstep module utilizing a Broyden–Fletcher–Goldfarb–Shannon (BFGS) optimizer with a 24 meV$Å^{-1}$ maximum force for convergence criteria.

(1) Benedek, P.; Wenzler, N.; Yarema, M.; Wood, V. C., Low temperature hydrothermal synthesis of battery grade lithium iron phosphate. *RSC Advances* **2017**, *7* (29), 17763-17767.

(2) Lutterotti, L.; Chateigner, D.; Ferrari, S.; Ricote, J., Texture, residual stress and structural analysis of thin films using a combined X-ray analysis. *Thin Solid Films* **2004**, *450* (1), 34-41.

(3) Azuah, R. T.; Kneller, L. R.; Qiu, Y.; Tregenna-Piggott, P. L. W.; Brown, C. M.; Copley, J. R. D.; Dimeo, R. M., DAVE: A Comprehensive Software Suite for the Reduction, Visualization, and Analysis of Low Energy Neutron Spectroscopic Data. *J. Res. Natl. Inst. Stan Technol.* **2009**, *114* (6), 341-358.

(4) Baroni, S.; de Gironcoli, S.; Dal Corso, A.; Giannozzi, P., Phonons and related crystal properties from density-functional perturbation theory. *Rev. Mod. Phys.* **2001**, *73* (2), 515-562.

(5) Kresse, G.; Furthmüller, J., Efficient iterative schemes for ab initio total-energy calculations using a plane-wave basis set. *Phys. Rev. B* **1996**, *54* (16), 11169-11186.

(6) Togo, A.; Tanaka, I., First principles phonon calculations in materials science. *Scr. Mater.* **2015**, *108*, 1-5.

(7) Perdew, J. P.; Ruzsinszky, A.; Csonka, G. I.; Vydrov, O. A.; Scuseria, G. E.; Constantin, L. A.; Zhou, X.; Burke, K., Restoring the Density-Gradient Expansion for Exchange in Solids and Surfaces. *Phys. Rev. Lett.* **2008**, *100* (13), 136406.

(8) Blöchl, P. E.; Jepsen, O.; Andersen, O. K., Improved tetrahedron method for Brillouin-zone integrations. *Phys. Rev. B* **1994**, *49* (23), 16223-16233.

(9) Vandevondele, J.; Krack, M.; Mohamed, F.; Parrinello, M.; Chassaing, T.; Hutter, J. Quickstep: Fast and Accurate Density Functional Calculations Using a Mixed Gaussian and Plane Waves Approach. *Comput. Phys. Commun.* **2005**, *167* (2), 103–128.

(10) Lippert, G.; Hutter, J.; Parrinello, M. A Hybrid Gaussian and Plane Wave Density Functional Scheme. *Mol. Phys.* **1997**, *92* (3), 477–488.

(11) VandeVondele, J.; Hutter, J. Gaussian Basis Sets for Accurate Calculations on Molecular Systems in Gas and Condensed Phases. *J. Chem. Phys.* **2007**, *127* (11)

(12) Hartwigsen, C.; Goedecker, S.; Hutter, J. Relativistic Separable Dual-Space Gaussian Pseudopotentials from H to Rn. *Phys. Rev. B* **1998**, *58* (7), 3641–3662.

(13) Sumita, M.; Tanaka, Y.; Ikeda, M.; Ohno, T., Theoretically Designed Li3PO4 (100)/LiFePO4 (010) Coherent Electrolyte/Cathode Interface for All Solid-State Li Ion Secondary Batteries. *J. Phys. Chem. C* **2015**, *119* (1), 14-22.

(14) Wang, L.; Zhou, F.; Meng, Y. S.; Ceder, G. First-Principles Study of Surface Properties of $LiFePO_4$: Surface energy, structure, Wulff shape, and surface redox potential. *Phys. Rev. B* 2007, *76* (16), 165435.

2. Preparation of the FePO4 particles via Delithiation

For our $FePO_4$ particles, we needed samples that were directly comparable to the LFP particles. To achieve these requirements, we electrochemically delithiated our LFP samples by making composite electrodes and cycling them in pouch cells. The samples were then washed in an Ar glovebox.

The LFP electrodes were prepared with 80wt% active material LFP, 10wt% Carbon black (Super C65), and 10wt% PVDF (Kynar HSV900) binder. To enable us to obtain enough delithiated LFP, we prepared four-layer pouch cells with copper foil as a counter electrode and a glass fiber sheet separating the LFP electrodes from the copper foil (**Figure S1a**). One electrical contact was then welded to the four cathodes and one to the four anode electrodes (**Figure S1b)** shows a top view image of the electrode stack with the welded contacts. The stack was then dried under vacuum in the antechamber of the glovebox at 120°C for a few hours. The stack was put into a polyethylene plastic bag to keep the electrolyte conserved around the electrodes and prevent electrical shorts and then into the aluminum pouch with three of four sides sealed. The electrolyte, a 1M solution of $LiPF_6$ in a 1:1 mixture ethylene carbonate and dimethyl carbonate (BASF), was then added into the plastic bag and the whole structure was then sealed and uniformly compressed.

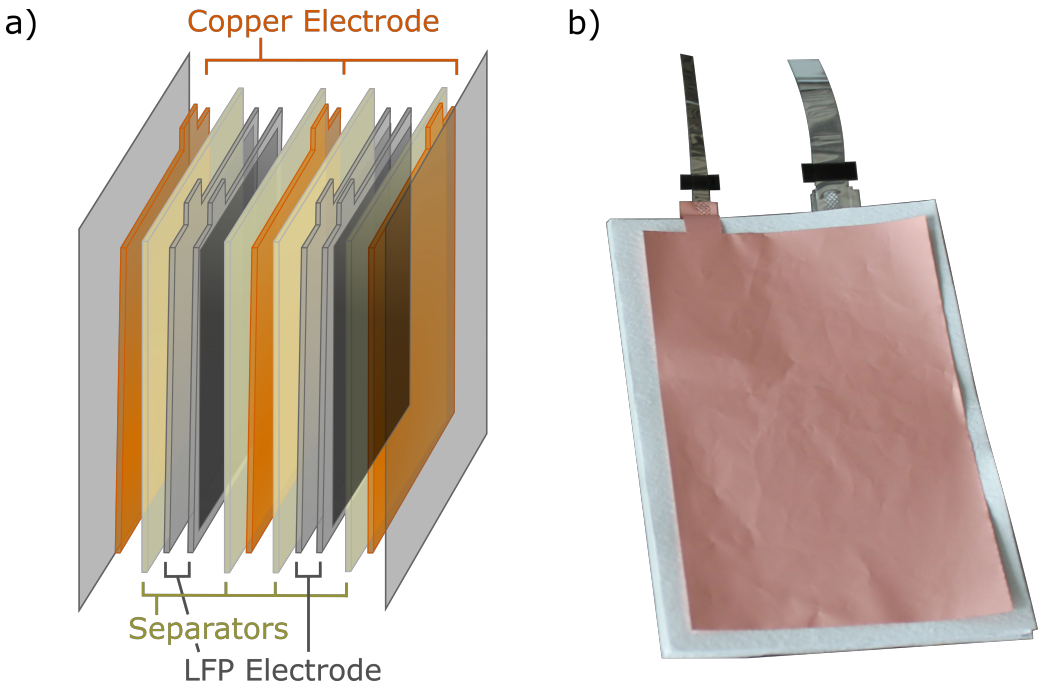

Figure S1. a) Schematic image of the stacking of the four-layer pouch cell before welding the tabs to a contact. b) Image of the stacked electrode with the welded contacts on the cathode and anode tabs.

The samples were then charged at C/50 to 4.2V followed with a potentiostatic step at that voltage, with the lithium from the LFP depositing directly on the copper foil. After charging, the pouch cells were transferred into the glovebox (**Figure S2a**), where they were cut open and the layers of the cell were carefully separated. The copper electrode and the separator showed that lithium dendrites had formed during the charging process (**Figure S2b**). The delithated electrode was then scratched from the aluminum current collector of the cathode and collected in a centrifuge tube (**Figure S2c, d**). NMP was added to the centrifuge tube to dissolve the PVDF, and the tube was sonicated in an oil-filled bath to facilitate this. The mixture was centrifuged to separate the light carbon black from the LFP. This process was then repeated until clean delithiated particles are is obtained at the bottom of the centrifuge tube (**Figure S2e**). The powder was analyzed by XRD and SEM imaging (**Figure S3**). The (020) peak indicated pure $FePO_4$, and in the "Meso" only a small peak of leftover LFP is observed (**Figure S3b**).

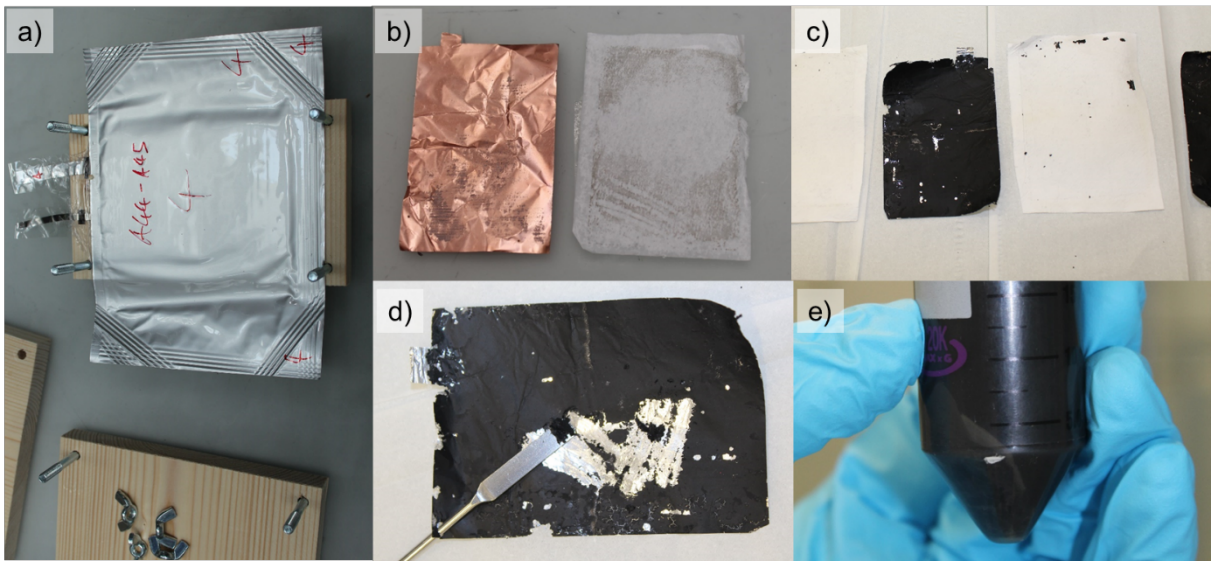

Figure S2. Preparation steps of the $FePO_4$ samples after cycling. a) Image of a cycled pouch cell. The wood plates are used to apply pressure on the pouch cell and the scotch tape around the contacts to avoid accidental short circuits during transfer to the glovebox. b) Image of the lithiated copper current collector and the glass fiber separator showing evidence of lithium dendrites. c) Image of the other side of the glass fiber separator and the LFP electrode. We observed no dendrites growing through the separator. d) Once the stacked pouch cell is disassembled, the electrode material is scratched from the electrode with a spatula and transferred in a centrifuge tube. e) After extensive washing and centrifuging, the dark brown LFP powder is separated from the PVDF and carbon black mixture and isolated.

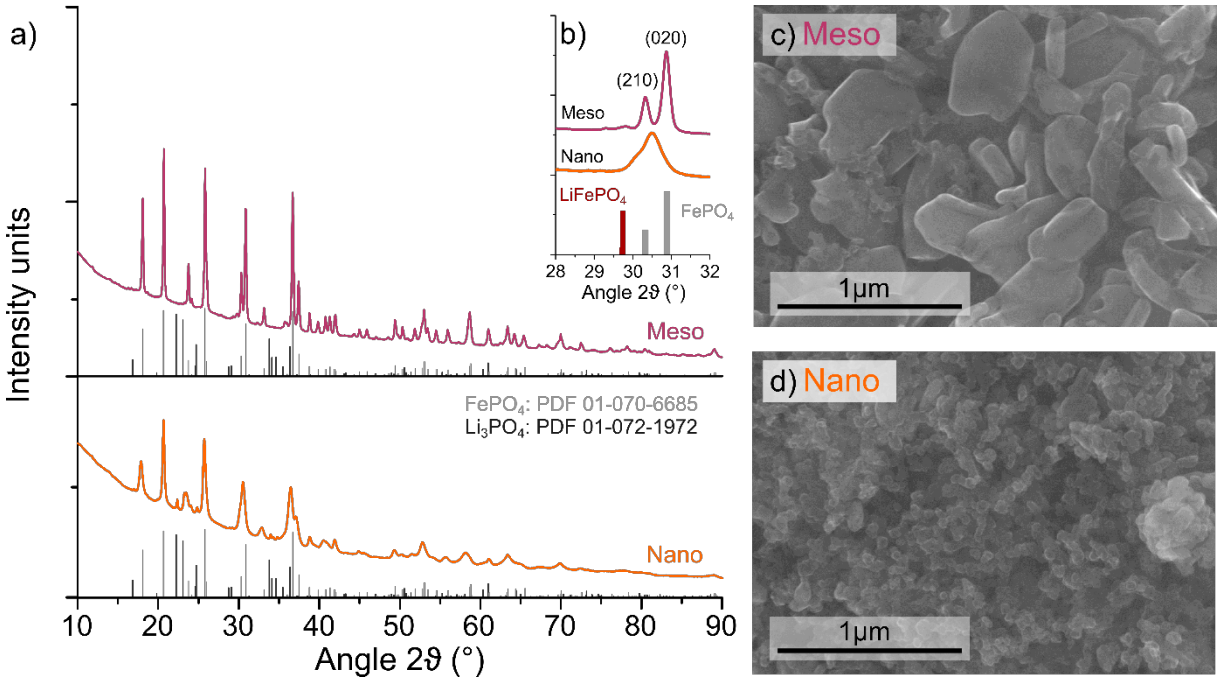

Figure S3. Analysis of delithiated of LFP. (a) Full XRD patterns of the "Meso" (top) and "Nano" (bottom) platelets after delithiation. The heterosite $FePO_4$ main phase and Li_3PO_4 impurity peaks is shown in gray. (b) A zoom in of the XRD spectra of the delithiated "Nano" and "Meso" samples in the region of (020) and (210) peaks. We find some residual LFP phase in the "Meso" particles. The LFP phase is not present in the "Nano" phase due to the reduction of the $LiFePO_4/FePO_4$ miscibility gap. SEM images of the (c) "Meso" and (d) "Nano" sample.

3. Carbon Coating: Raman Spectrum

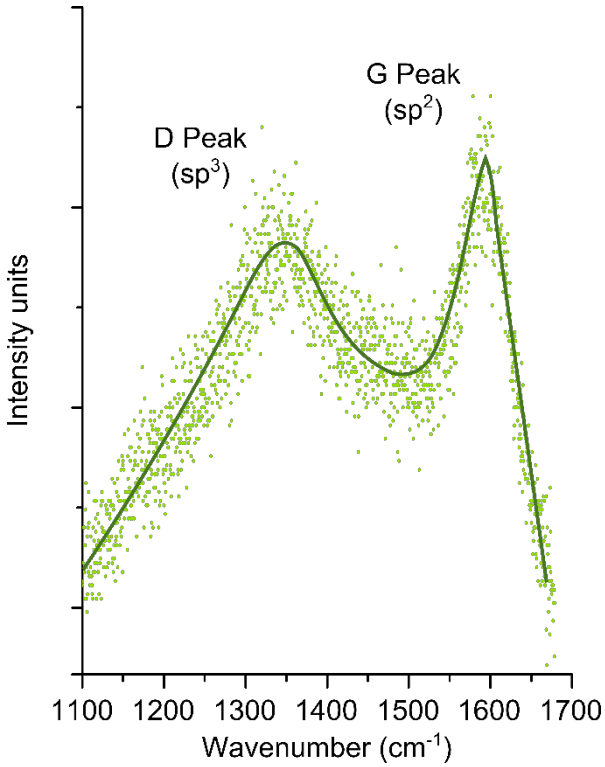

Figure S4. Raman spectrum of carbon bonds in the $LiFePO_4$ coating. We find a clear separation of the D peak and the G peak.

4. LFP Platelets: TEM Images

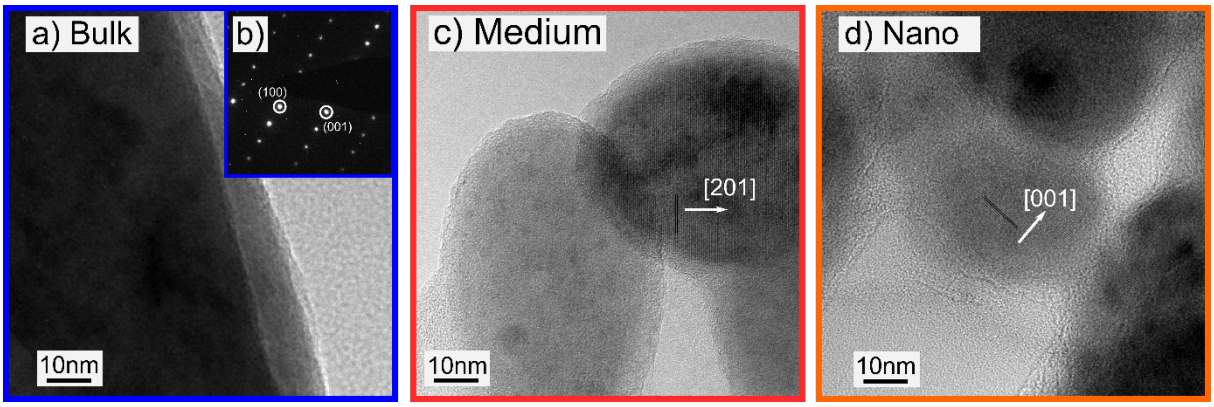

Figure S5. a) TEM image of the "Bulk" sample with b) the selected area diffraction pattern. c),d) TEM images of the "Medium" and "Nano" particle, respectively with the crystallographic [201] or [001] direction depicted, respectively.

5. LFP Platelets: Size Distribution

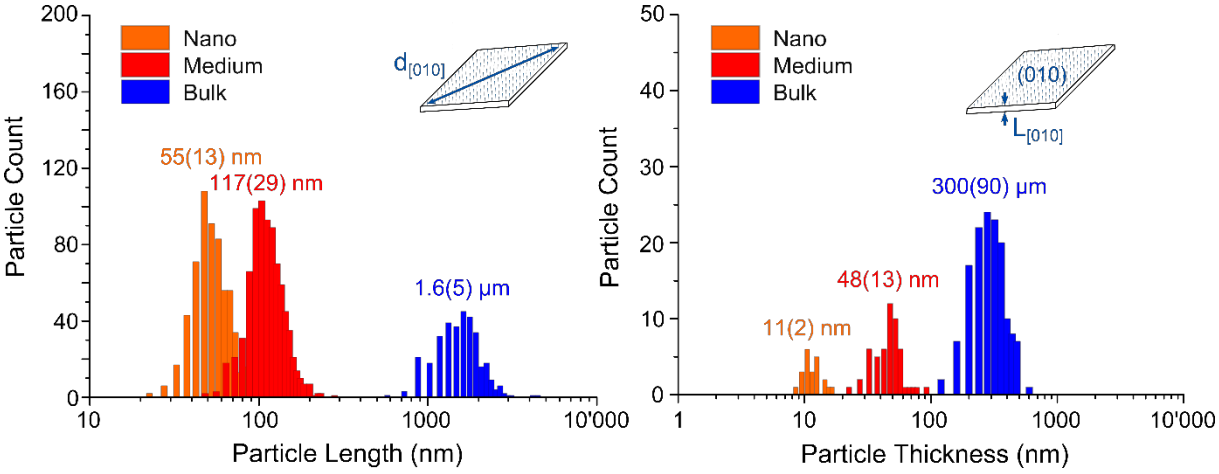

Figure S6. Size distribution of the LFP samples used for the INS measurements. Particle (a) length and (b) thickness distributions.

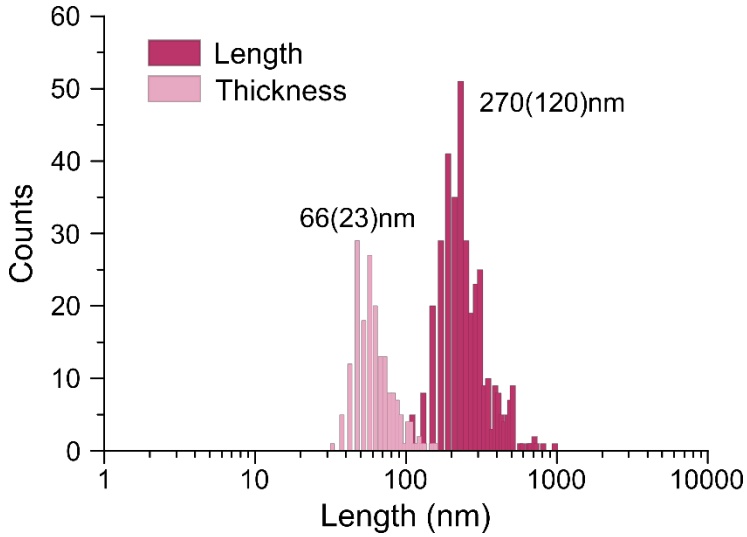

Figure S7. Particle size distribution of the "Meso" sample.

6. Electrochemical characterization

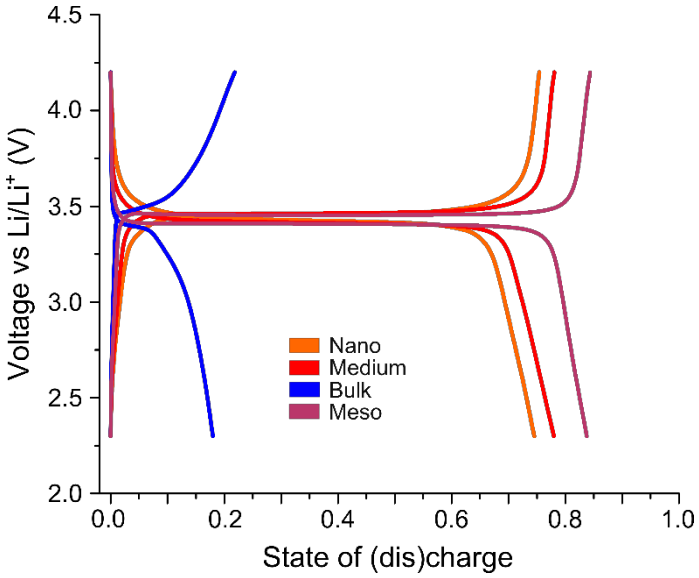

Figure S8. Galvanostatic (dis)charge curves of the LFP samples used in this study for a rate of C/10 corresponding to a specific current of 17mA/g. The galvanostatic curves here are from the second C/10 cycle.

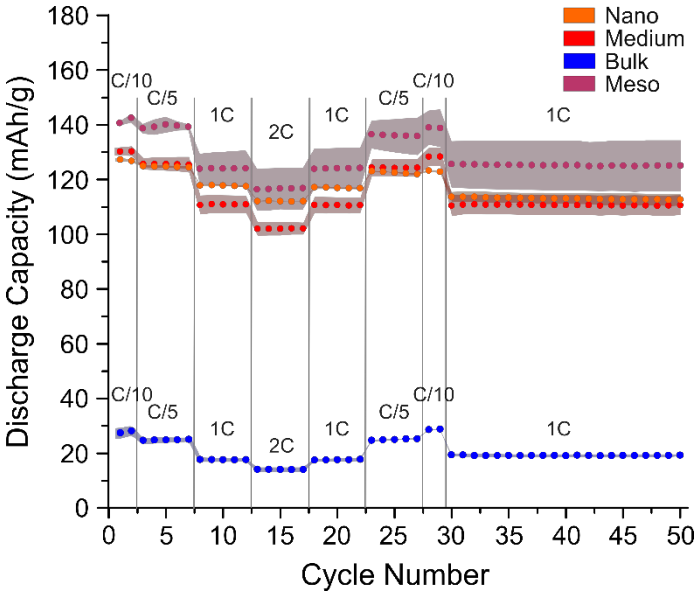

Figure S9. Rate-dependent discharge capacity of the samples used in this study. The dots show the average capacity from at least three cells from different slurries with the standard deviation depicted by the shading. The given rate was used for both charge and discharge.

7. LFP Platelets: Size calculations

From the channel length $L_{[010]}$ (equal to the particle thickness) and the platelet diameter $d_{(010)}$, we calculate size parameters P such as the aspect ratio and the percentage of atoms on the (010) surface. The error of all those parameters is then obtained via a first order Taylor expansion of the standard deviations of $L_{[010]}$ and $d_{(010)}$ (1).

$$dP\left(L_{[010]}, d_{(010)}\right) = \sqrt{\left(\frac{\partial P}{\partial L_{[010]}}\right)^2_{d_{(010)}}}\, dL_{[010]} + \sqrt{\left(\frac{\partial P}{\partial d_{(010)}}\right)^2_{L_{[010]}}}\, d(d_{(010)}) \tag{1}$$

a) Aspect ratio

We define the aspect ratio of the platelet particle, AR, as the ratio between $d_{(010)}$ and the channel length $L_{[010]}$. With (1), the error of the aspect ratio, dAR, is then given by (3).

$$AR = \frac{d_{(010)}}{L_{[010]}} \tag{2}$$

$$dAR = \frac{d(d_{(010)})}{L_{[010]}} + \frac{d_{(010)}}{L^2_{[010]}}\, dL_{[010]} \tag{3}$$

b) Atoms on (010) surface

To calculate the relative ratio of atoms on the (010) surface, n(010), we considered all atoms in the topmost unit cell of the (010) surface. Therefore, we calculated how many unit cells appeared along the b direction. This reduces the calculation to a one-dimensional problem and we can simply divide the two surface unit cells by all the unit cells along the b direction (4) with the error $dn_{(010)}$ (5).

$$n_{(010)} := \frac{N_{(010)}}{N_{tot}} = \frac{2b}{L_{[010]}} \tag{4}$$

$$dn_{(010)} = \frac{2b}{L_{[010]}^2} dL_{[010]} \tag{5}$$

c) (010) to entire surface ratio

The geometric (010) surface ratio, $a_{(010)}$ was calculated assuming that the particles are disks with a circular (010) face having diameter $L_{(010)}$. This assumption is motivated by the fact that the edges in the "Nano", "Medium", and "Meso" particles are rounded after annealing. For the diamond shaped "Bulk" sample this assumption is less accurate. The ratio of the top surface and the entire surface is:

$$a_{(010)} := \frac{A_{(010)}}{A_{tot}} = \frac{2\pi\left(\frac{d_{(010)}}{2}\right)^2}{\left(2\pi\left(\frac{d_{(010)}}{2}\right)^2 + \pi d_{(010)} L_{[010]}\right)} \tag{6}$$

$$= \frac{d_{(010)}}{d_{(010)} + 2L_{[010]}} \tag{7}$$

$$da_{(010)} = \frac{2L_{[010]}\, d(d_{(010)}) + 2d_{(010)} dL_{[010]}}{\left(d_{(010)} + 2L_{[010]}\right)^2} \tag{8}$$

d) Atoms on other surfaces

The calculation of the percentage of atoms on other surfaces than the [010] surface is more complex. Again, we assume circular disk shaped platelets with diameter $L_{(010)}$. The assumption enables us to study a two-dimensional cut along the (010) surface and measure the number of

unit cells along the circle edge. As for the (010) surface, the number of atoms on the edge scales with the number of edge unit cells. The calculation of the edge unit cell number, however, is more difficult than before due to the orthorhombic unit cell of LFP (which in our 2D picture becomes rectangular). Since the lattice vectors c and a do not match, a different amount of unit cells will be found along every direction of the circular disk. This is equivalent to the case of having an ellipse with a square unit cell, which makes calculations easier (**Figure S10**). Therefore, we apply the coordinate transformation

$$\frac{L_{(010)}}{2} \equiv r, a, c \ \rightarrow r_a, r_c \tag{9}$$

with

$$r_i = \frac{r}{i} = \frac{L_{(010)}}{2i}, \qquad i \in \{a, c\}, \tag{10}$$

that transforms the circular disk in an ellipse with the two semi-minor axes r_a and r_c. These axes represent the number of unit cells along these directions. Therefore, the number of surface atoms not on (010) is given by the ratio of the transformed ellipse circumference, C_{ell}, and the ellipse area A_{ell}.

$$\frac{N_{surf\backslash(010)}}{N_{tot}} = \frac{C_{ell}}{A_{ell}} = \frac{r_a \int_0^{2\pi} \sqrt{1 - \left(1 - \frac{{r_c}^2}{{r_a}^2}\right)\cos^2\varphi}\, d\varphi}{\pi r_a r_c} \tag{11}$$

Rearranging and replacing r_a and r_c using (11) leads to (13) with the error (14). The circumference integral is then numerically evaluated.

$$\frac{C_{ell}}{A_{ell}} = \frac{2c \int_0^{2\pi} \sqrt{1 - \left(1 - \frac{a^2}{c^2}\right)\cos^2\varphi}\, d\varphi}{\pi L_{(010)}} \tag{12}$$

$$d\left(\frac{C_{ell}}{A_{ell}}\right) = \frac{2c\int_0^{2\pi}\sqrt{1-\left(1-\frac{a^2}{c^2}\right)\cos^2\varphi}\,d\varphi}{\pi L_{(010)}^2}\,dL \tag{13}$$

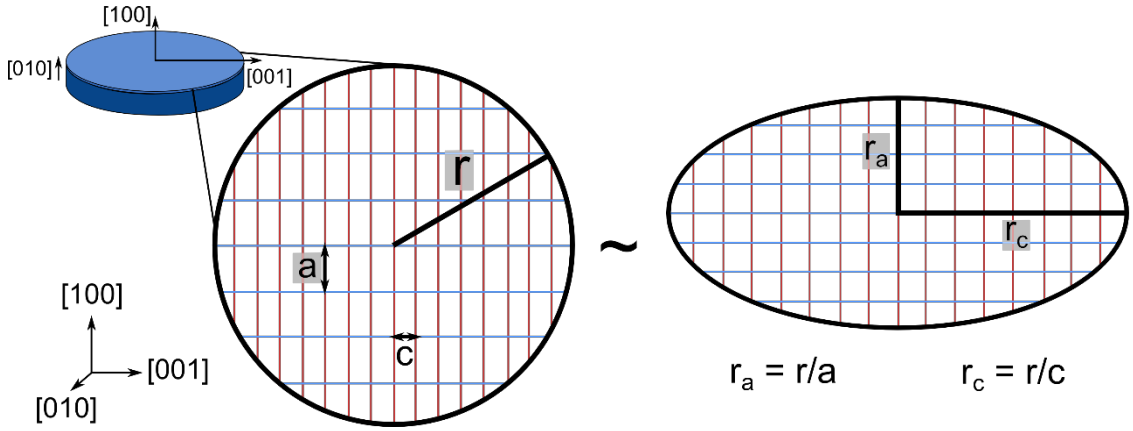

Figure S10. Schematic image of the LFP disk used for the calculations and its transformation to an ellipse with a square lattice.

8. Neutron Scattering Data: Frame Overlap and Paramagnetic Scattering

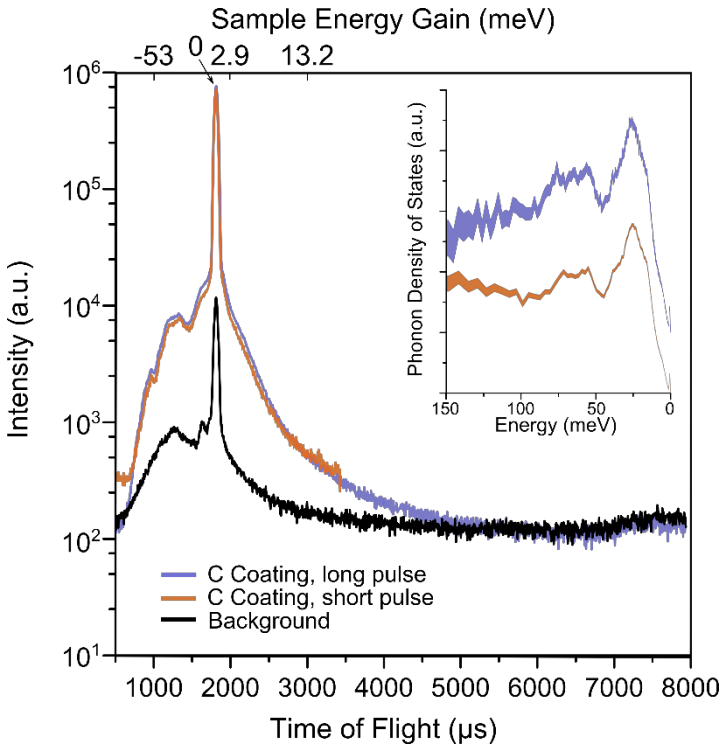

Figure S11. Time-of-flight spectrum of the nanoparticle sample. Due to beam time restrictions, a short time of flight pulse of 4ms was chosen. On such a short pulse, neutrons from the previous pulse reach the sample at the start of the next pulse. This effect is called frame overlap and leads to an artifact in the PDOS (see inset) where the PDOS seemingly increases at high energy transfers. Comparing the PDOS measured on "Nano" LFP with (orange) and without (blue) the frame overlap, shows that frame overlap does not affect the shape of the PDOS in the important energy range in this study (50-100meV).

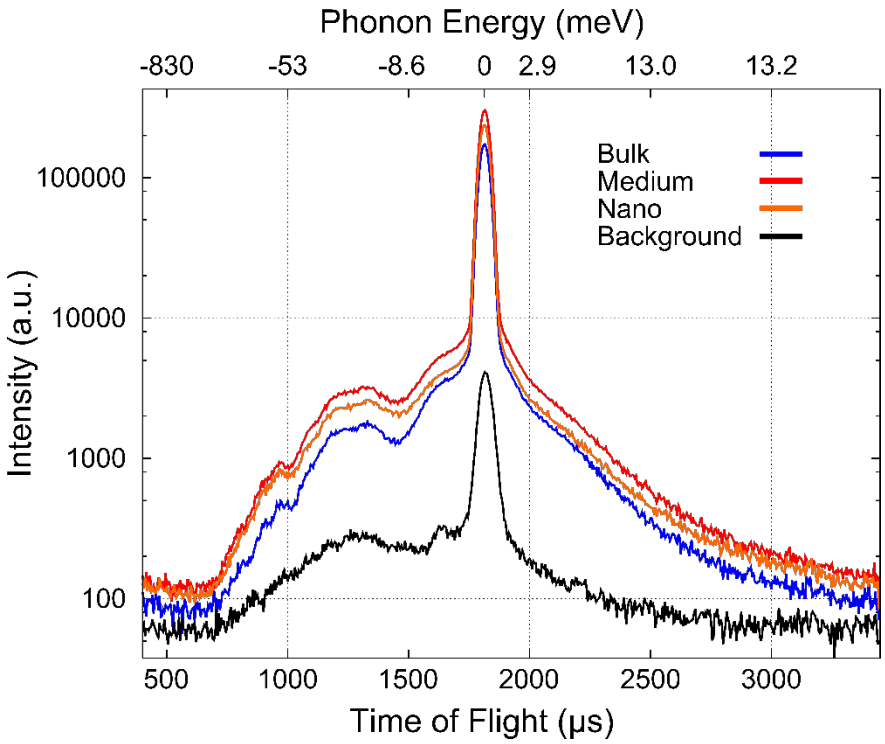

Figure S12. Time-of-flight spectra of the $LiFePO_4$ samples measured in this study. As mentioned above, all samples have a short pulse, leading to significant frame overlap.

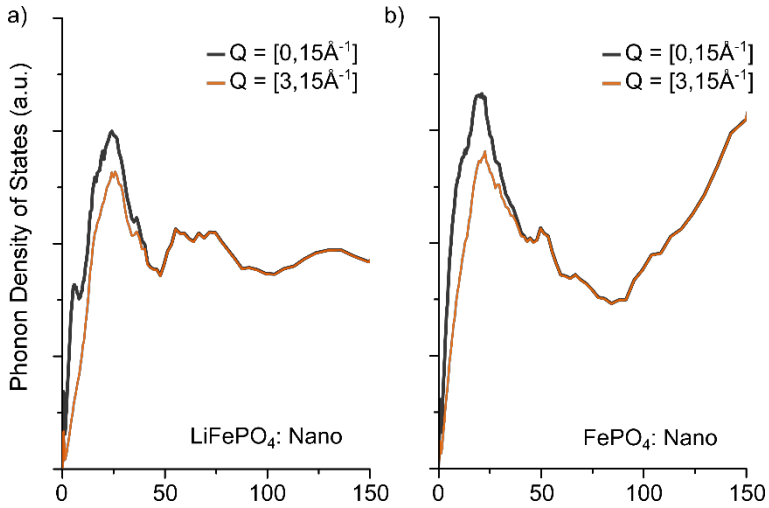

Figure S13. Phonon density of states spectra of a) "Nano" LFP and b) "Nano" $FePO_4$ as a function of selected scattering vectors Q. The influence of paramagnetic scattering can be significantly reduced by analyzing a restricted Q range above 3 $Å^{-1}$ (orange).

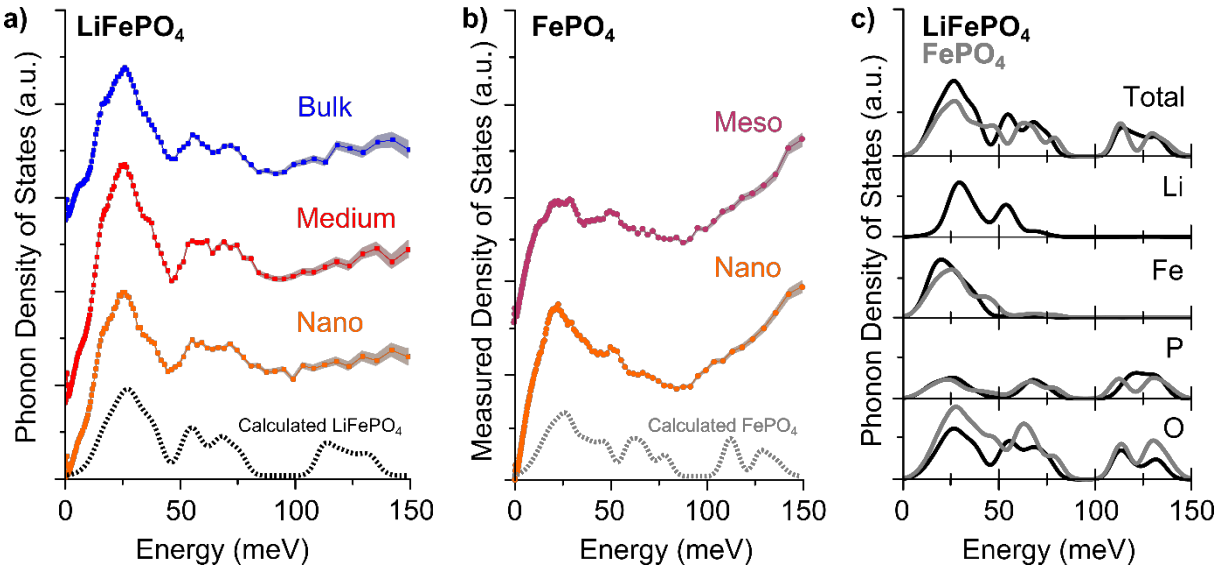

Figure S14. The experimentally-measured phonon density of states for **a)** $LiFePO_4$ (LFP) and **b)** delithiated LFP (i.e., $FePO_4$) samples of different sizes. The shading around the points indicates the error of the measurement. The dashed lines show the calculated phonon density of states. **c)** Calculated total and elemental partial phonon density of states of LFP (black) and $FePO_4$ (gray) from bulk density functional theory simulations.

9. Impurity and Defect analyses

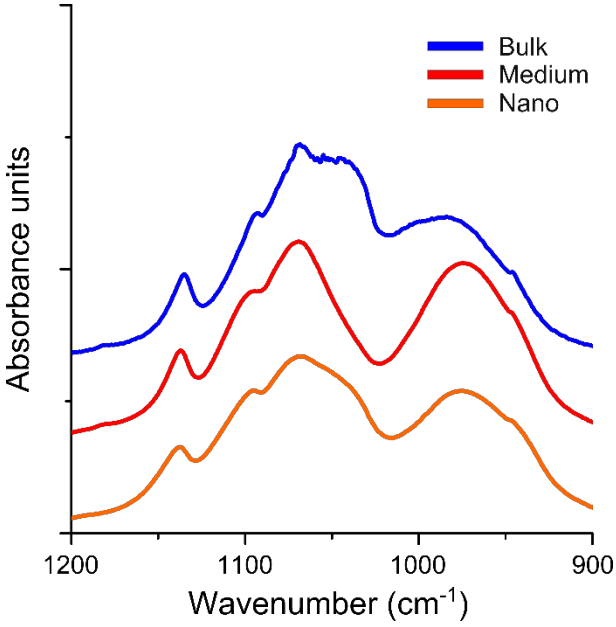

Figure S15. FTIR spectra in the P-O vibrational range of the "Nano", "Medium", and "Bulk" samples show that the right-most peak is positioned at around 980cm^{-1}, suggesting the same antisite defect concentration in the three samples. Note, that the Li_3PO_4 impurity in the "Nano" sample leads to a shoulder at 1050cm^{-1}.

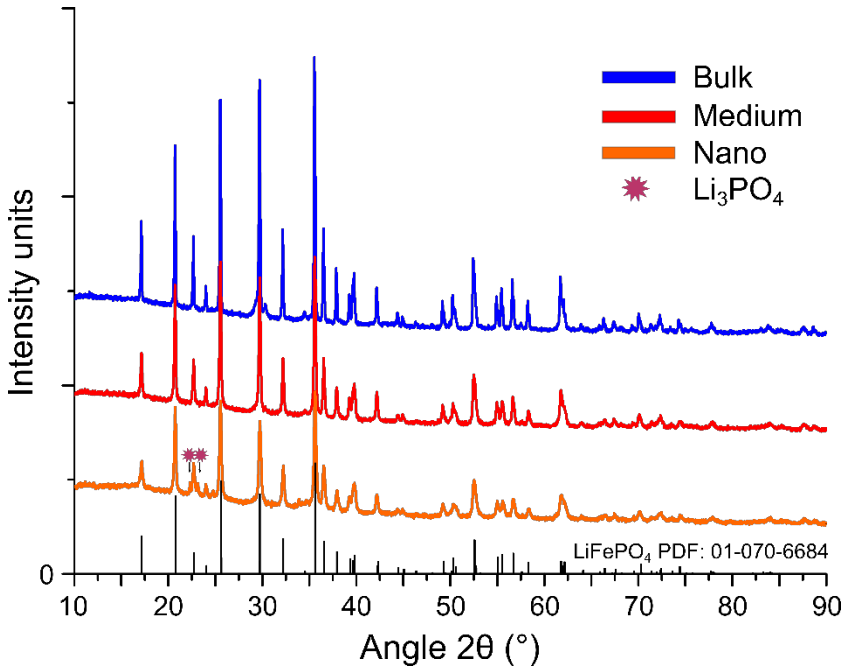

Figure S16. X-ray diffraction spectra of "Bulk", "Medium", and "Nano" LFP. We find that the samples are single phase $LiFePO_4$ except for the Li_3PO_4 impurity in the "Nano" samples (marked with an asterisk).

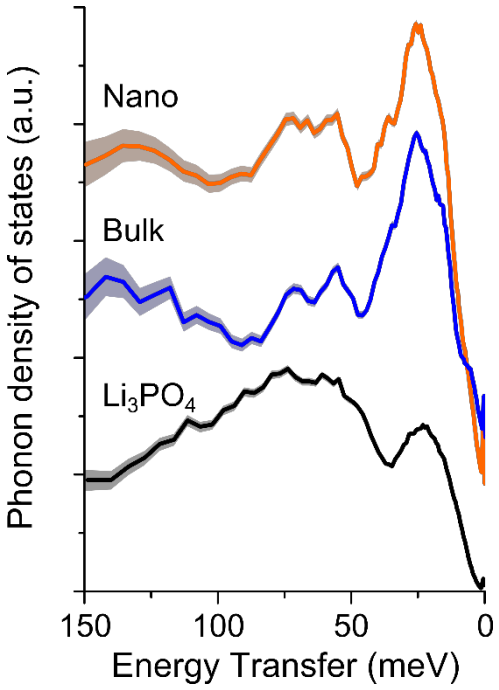

Figure S17. Comparison of phonon density of states of the "Nano" and "Bulk" samples with the phonon density of states of $^7Li_3PO_4$ spectrum obtained from INS measurements. Note the very broad phonon mode in the range of 50-100meV in Li_3PO_4 which is almost constant in the energy range of interest in this study.

10. Rietveld refinements

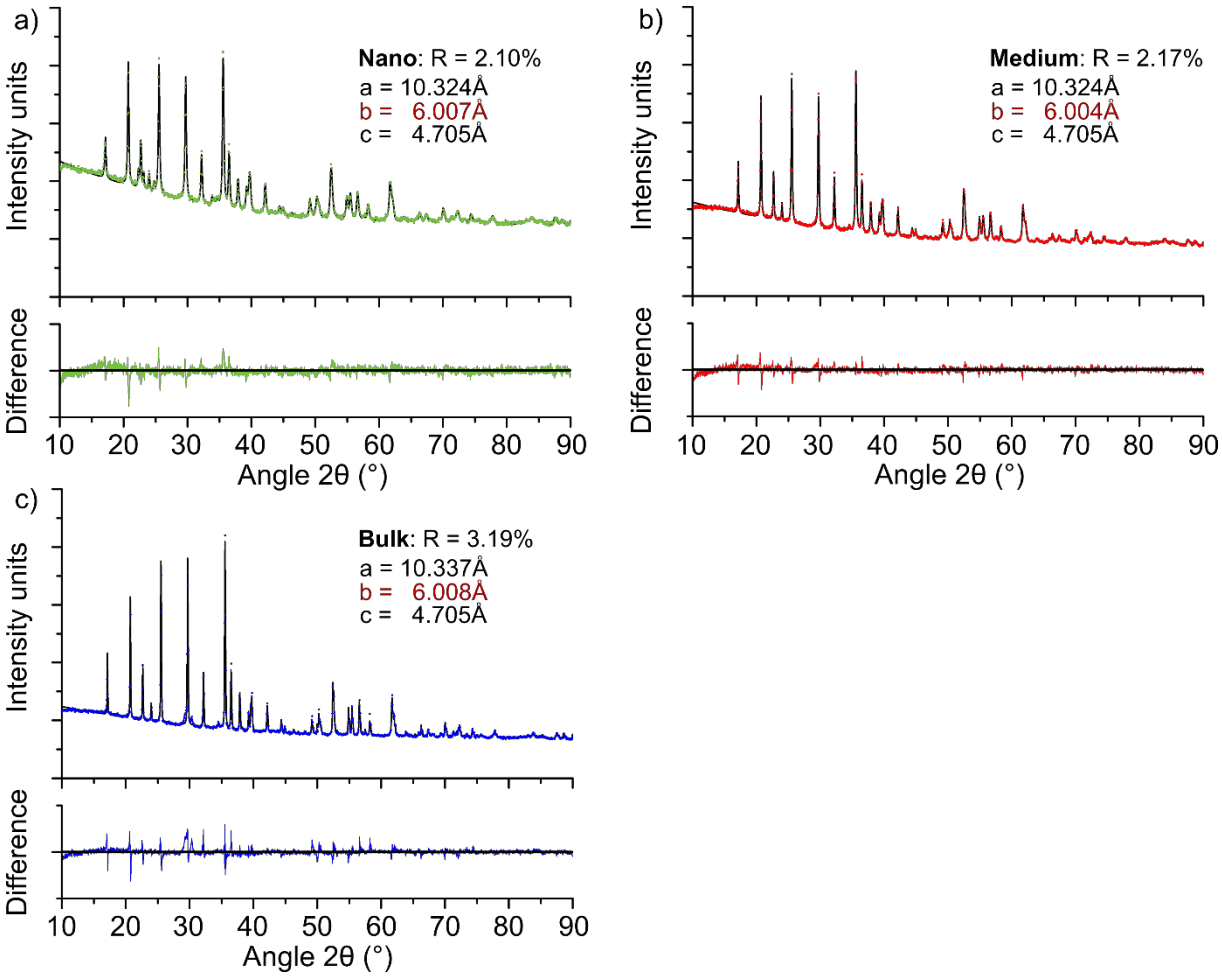

Figure S18. Rietveld Refinements of the "Bulk", "Medium", and "Nano" $LiFePO_4$ samples used in this study. For all the three samples the unit cell volume does not change significantly, indicating a similar defect concentration and small strain effects.

11. DFT slabs used for the calculations

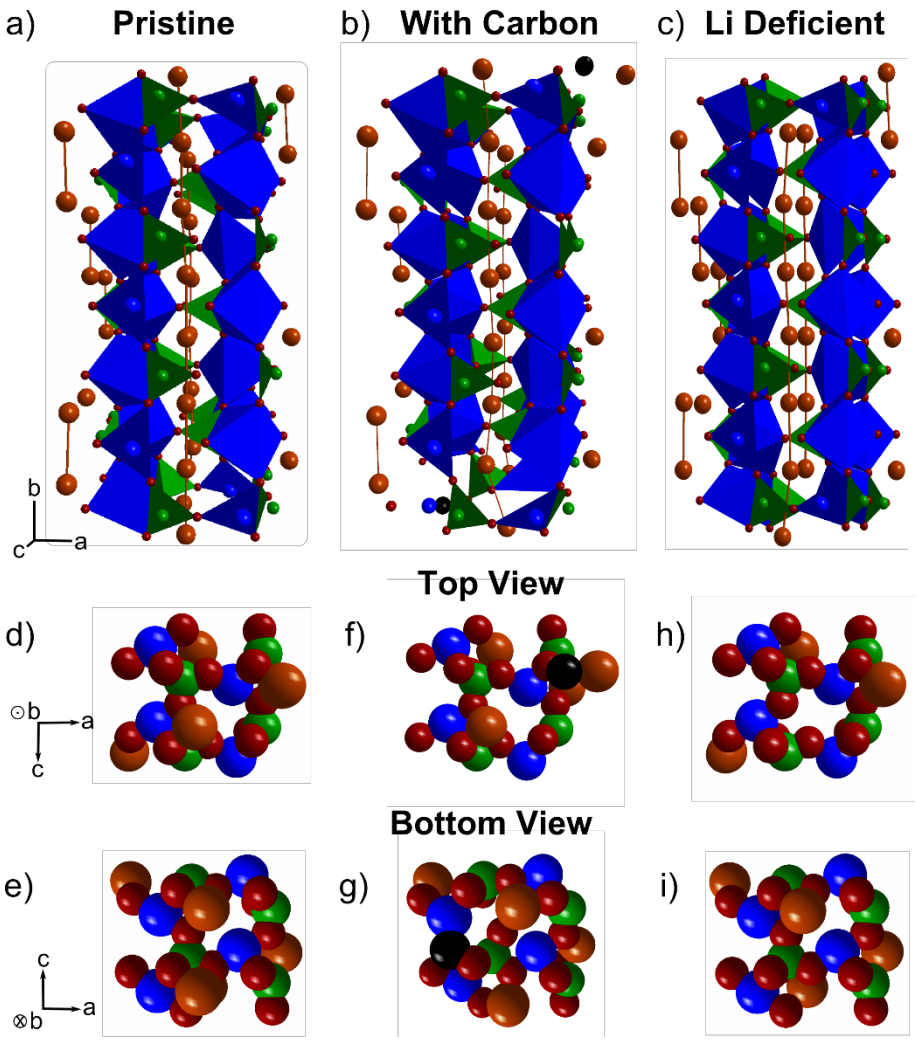

Figure S19. Schemes of the slabs used for the CP2k calculations after their geometrical optimization. a)-c) Full slabs of the pristine LFP slab, the slab with one carbon atom on each side, and the Li deficient slab, respectively. d)-f) Top view of the slab for each of the three cases. g)-i) Bottom view of the slab for each of the three cases.

12. DFT bond lengths: Distributions

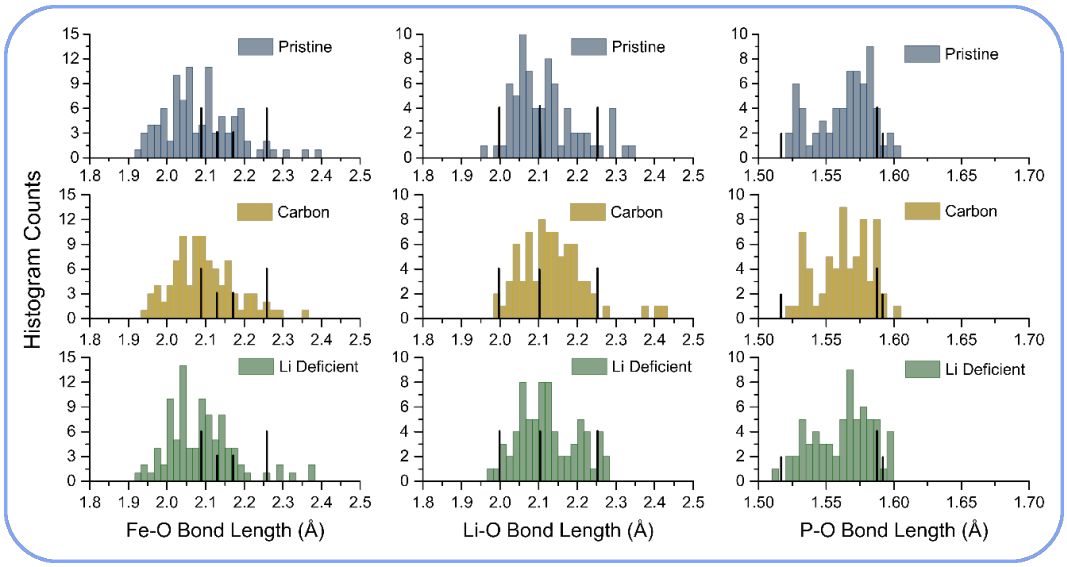

Figure S20. Histograms of the bond lengths in the interior of the LFP slabs. Black bars mark the bond lengths obtained from the Rietveld refinement of the "Bulk" LFP sample.

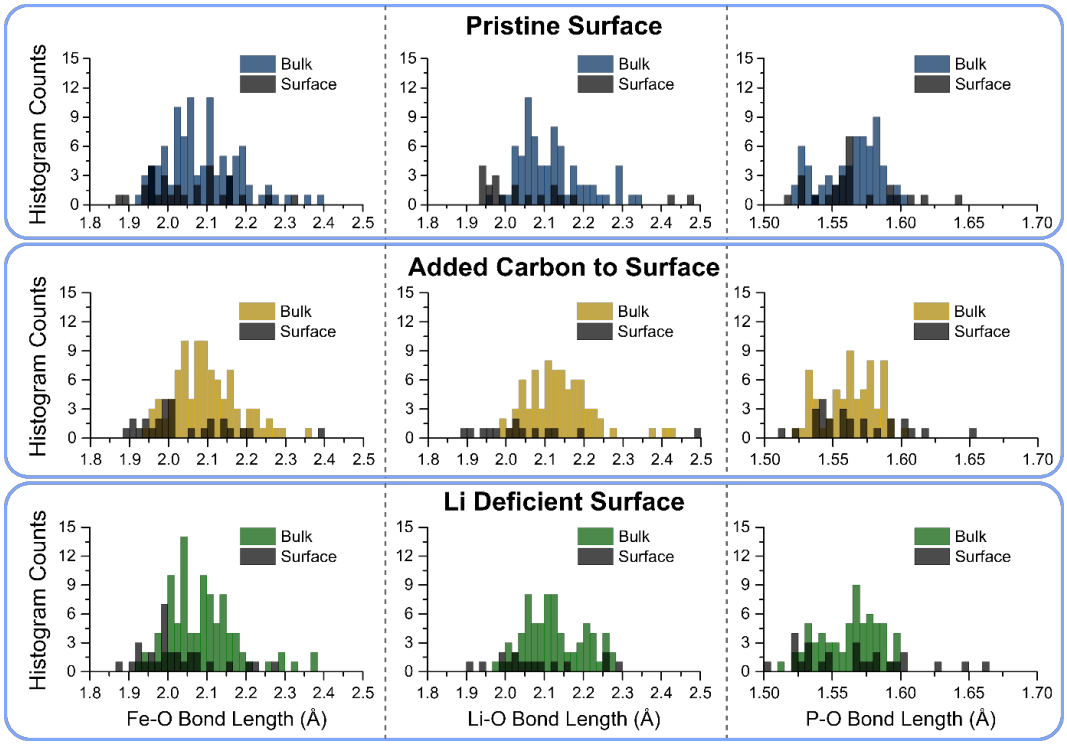

Figure S21. Comparison of the bulk (colored) and the surface bond lengths (dark) of the slabs for the three surface terminations (vacuum, carbon-coated, and lithium deficient). The distribution of bond lengths broaden and, in the case of Li-O and Fe-O bonds, shift towards smaller energies.

Table S2. Overview of the LFP unit cell parameters and average bond lengths.

	a (Å)	b (Å)	c (Å)	Li-O (Å)	P-O (Å)	Fe-O (Å)
Inner Slab DFT	9.910	6.095	4.636	2.116	1.563	2.088
Bulk DFT	10.256	5.989	4.689	2.133	1.554	2.142
“Bulk”	10.337	6.008	4.705	2.119	1.570	2.165